Biosensors and Bioelectronics 141 (2019) 111473

Contents lists available at ScienceDirect

Biosensors and Bioelectronics

journal homepage: www.elsevier.com/locate/bios

Tandem catalysis driven by enzymes directed hybrid nanoflowers for on-site ultrasensitive detection of organophosphorus pesticide

Rui Jin[a], Deshuai Kong[a], Xu Zhao[a], Hongxia Li[a], Xu Yan[a,*], Fangmeng Liu[a], Peng Sun[a], Dan Du[b], Yuehe Lin[b], Geyu Lu[a,**]

[a] State Key Laboratory on Integrated Optoelectronics, Jilin Key Laboratory on Advanced Gas Sensor, College of Electronic Science and Engineering, Jilin University, Changchun, 130012, People's Republic of China
[b] School of Mechanical and Materials Engineering, Washington State University, Pullman, WA, 99164, United States

ARTICLE INFO

Keywords:
Pesticides
Point-of-care detection
Organic-inorganic hybrid nanoflowers
Peroxidase activity
Dual-readout strategy

ABSTRACT

Accurate analysis of organophosphate pesticides (OPs) with portable devices remain an elusive goal that have received widespread investigative attention in the areas of environmental contamination and disease prevention. Herein, using all-in-one enzyme-inorganic hybrid nanoflowers (ACC-HNFs) to fabricate high-performance artificial enzyme cascade system, we established a sensitive and affordable lab-on-paper biosensor. This biosensor incorporated disposable screen-printed carbon electrode (SPCE) and colorimetric test strips, which enabled the dual-modal readout (electrochemical and colorimetric signal) for on-site monitoring of OPs, achieving an "on-demand" tuning of the detection performance. Using paraoxon as a model analyte, the ACC-HNFs-based lab-on-paper platform could reach a limit of detection down to the femtogram/mL level (6 fg mL^{-1}). Meticulous design of ACC-HNFs provided a versatile approach for constructing artificial enzyme as a recognizer and amplifier to fill the gap in constructing robust artificial enzyme systems which can be used for on-site contamination monitoring and biological diagnosis.

1. Introduction

Organophosphate pesticides (OPs) are strictly controlled in modern agriculture because they can cause persistent damage to public health, even at trace amount (Palmer et al., 2013; Pang et al., 2015; Yan et al., 2018a). To prevent OPs contamination effectively, rapid and accurate identification of OPs residues in agricultural products has become increasingly significant for the protection of consumer health (Aragay et al., 2012; Maliyekkal et al., 2013; Yan et al., 2018b). Although chromatography (Zhao et al., 2018) and mass spectrometry (Cequier et al., 2016) are widely used for the detection of OPs, these techniques still have some disadvantages, such as time-consuming procedures, sophisticated instrumentation, and labor-intensive, which make them unsuitable for on-site monitoring (Nasir et al., 2017; Szyszko et al., 2015). Considerable strategies have been developed for real-time sensing of OPs (Shen et al., 2018; Wang et al., 2019; Yan et al., 2017; Zou et al., 2018), among which electrochemical sensors possess advantages of economy, simplicity, and miniaturization capability in point-of-care testing (POCT) field (Ge, L. et al., 2012; Liebes-Peer et al., 2014). The most popular electrochemical strategy for monitoring OPs is indirectly carried out by testing enzyme activity loss of cholinesterase (ChE) (Chen et al., 2017; Gupta et al., 2011; Khare et al., 2012; Winrow et al., 2003). Although enzyme-based electrochemical biosensors are featured with acceptable selectivity and sensitivity, their drawbacks are also conspicuous. One challenge of the fabrication of an enzyme-based electrochemical biosensor is that enzymes as signal-amplifier are unstable and vulnerable to environment, further influence the stability performance of sensor (Kaur and Prabhakar, 2017). In addition, the detection limits of these biosensors are usually hard to be improved to the level of picogram/mL, which is unable to satisfy the monitoring requirements of low-abundant targets (Yang et al., 2011). More importantly, the signal output is confirmed only through electrochemical workstation-processed electric signal to quantitative analysis of target pesticide. Such a single-modal readout makes the discrimination and elimination of signal noises induced by matrix or interferents difficult. Accordingly, obtaining new enzyme amplification protocols for routine enzyme-based electrochemical biosensors to circumvent these shortcomings possess urgently desire. Significant endeavors have been undertaken to enhance output signal by investigating nanomaterials as carriers for enzyme immobilization, because immobilizing enzymes

* Corresponding author.
** Corresponding author.
E-mail addresses: yanx@jlu.edu.cn (X. Yan), lugy@jlu.edu.cn (G. Lu).

https://doi.org/10.1016/j.bios.2019.111473
Received 6 May 2019; Received in revised form 20 June 2019; Accepted 23 June 2019
Available online 26 June 2019
0956-5663/

could enhance enzyme stability in operational conditions (Uth et al., 2014). For instance, two-dimensional transition metal dichalcogenides were employed as nanocarriers to immobilize enzyme via chemical crosslinking, which can increase the stability of enzyme. Cui et al. developed a multi-layered sol-gel matrix for loading AChE by layer-by-layer casting and electrodeposition, which showed high stability and reproducibility (Cui et al., 2018). Besides the benefits brought by enzyme immobilization, it is necessary to recognize that the performance of enzyme activity can suffer changes upon immobilization. The current nanomaterials-based enzyme immobilization takes place during the complex process of covalent linkage or sol-gel synthesis, which may lead to denaturation of enzyme (Chen and Chatterjee, 2013; Si et al., 2011). Moreover, those nanomaterials with the relatively low loading capacity of enzyme hinder the use of platform.

The core protocol for enhancing stability and sensitivity of enzyme-based electrochemical biosensors includes not only maintain the bioactivity of enzyme but also carry numerous of enzymes (Tang et al., 2011). Organic-inorganic hybrid nanoflowers (HNFs), the three-dimensional shape of flower-like hybrid materials, have aroused extensive attentions especially for enzyme immobilization applications (Ge, J. et al., 2012; Ye et al., 2016). Such HNFs exhibited two intrinsic advantages: (1) The large surface area offers more active sites to provide a guarantee for more enzyme loading (2) Enzymes can be adsorbed into the gap of petals, rather than dangling on the surface of the HNFs, contributing to maintain the stability of the enzyme and reduce leaching during recycling. Thus, HNFs as enzyme carriers hold great promise in the field of sensing (Wu et al., 2018; Yu et al., 2017). More interestingly, Cu-based HNFs can possess unique peroxidase-like activity, which catalyze hydrogen peroxide to produce •OH (Huang et al., 2015; Zhu et al., 2018). These Cu-based HNFs scaffolds provided a considerable opportunity for integrating natural enzyme and nanozyme, which in principle exhibit multiple cascade catalysis (Miao et al., 2018).

Inspired by the aforementioned developments, we exploited the HNFs to fabricate paper-based biosensor with electrochemical signal output and complementary colorimetric readout for on-site monitoring of OPs. In order to achieve this design, all-in-one enzyme-inorganic hybrid nanoflowers (ACC-HNFs) were chosen as the support material for immobilizing AChE and choline oxidase (ChO) on the surface of detection zone IV (Scheme 1). As-synthesized ACC-HNFs composite with activity of natural enzymes (AChE and ChO) could catalyze the substrate acetylcholine (ACh) to generate H_2O_2. Then the peroxidase-like activity of ACC-HNFs toward the catalytic oxidation of 3,3′,5,5′-tetramethylbenzidine (TMB) with the help of enzymatic product H_2O_2. ACC-HNFs not only possess unique mimic enzyme-like activity and natural enzyme property to catalyze coloration of the chromogenic substrate, but also amplify the electrical signals by tandem catalysis reactions. As indicated in Scheme 1, after introduced paraoxon to the detection zone IV, the test strip was folded in order from regions I to II to III, and then a discernible colorimetric signal was observed in the observation zone. Subsequently, the entire test strip was folded above the electrode for amperometric measurement. By using this dual-readout platform, a rapid and preliminary qualitative analysis of OPs can be performed with naked eyes, and accurately quantitative detection result can be further achieved with a portable electrochemical workstation.

2. Experimental section

2.1. Materials and instruments

$KMnO_4$, AChE, ChO, ACh, and acetylthiocholine (ATCh) were purchased from Ryon Biological Technology Co., Ltd. (Shanghai, China). Tris-HCl buffer solution, acetate buffer solution, TMB, 5,5-dithiobis (2-nitrobenzoic acid) (DTNB), and dimethylsulfoxide (DMSO) were obtained from Sigma-Aldrich reagent Co., Ltd. (St. Louis, MO, USA). The UV–Vis absorbance measurements were obtained on a UV-2550 spectrometer (Shimadzu). Electrochemical experiments were operated with electrochemical workstations (Vertex. One. EIS, Ivium, Netherlands) at room temperature. Screen-printed carbon electrode (SPCE) was bought from MM Electronic Technology Co., Ltd. (Shanghai, China). Prior to electrochemical measurements, SPCE was washed separately with ethanol and deionized water, dried by nitrogen later. The detailed microstructures of the samples were analyzed with JEM-2100 transmission electron microscope (TEM) and JEM-7500 scanning electron microscope (SEM). X-ray diffraction (XRD) analysis was used a Bruker AXS D8 Advance Powder X-ray diffractometer. FT-IR spectra analysis was collected using a Nicolet 6700 FT-IR spectrometer (Thermo) in reflectance mode. Thermal gravimetric analysis (TGA) was carried out under a stream of nitrogen at a heating rate of 10 °C min^{-1} from 30 °C to 800 °C using a Hi-Res TA Instruments Model 2901.

2.2. Preparation of the AChE/ChO/$Cu_3(PO_4)_2$-HNFs

Typically, 30 μL of 200 mmol L^{-1} PBS (pH 8.0) contained 50 μL of AChE (1.0 U mL^{-1}) and 50 μL of ChO (2.0 U mL^{-1}) was added to

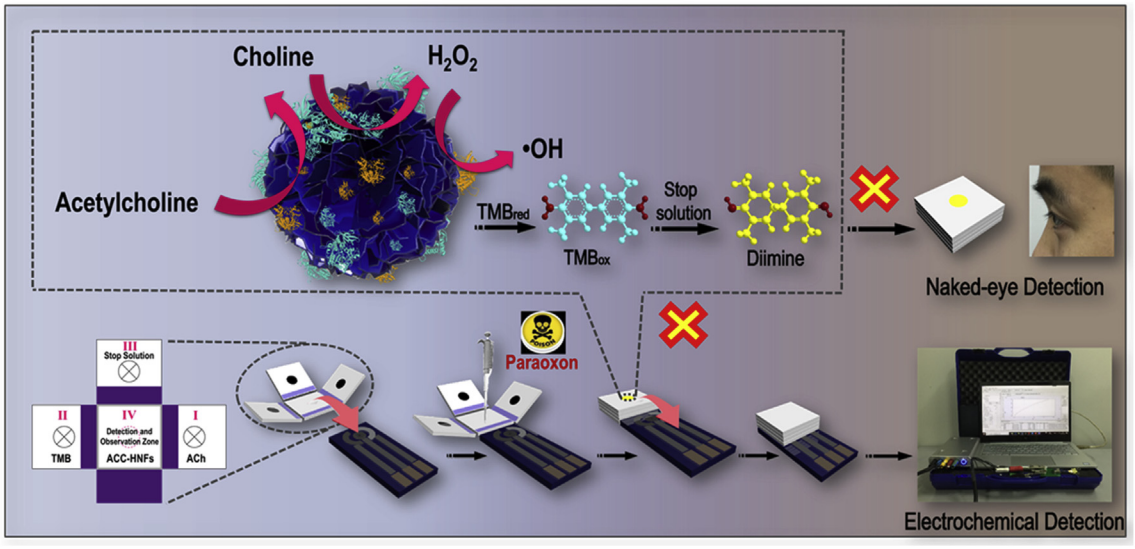

Scheme 1. Schematic illustration of the proposed dual-modal paper-based biosensor.

845 μL deionized water, then 25 μL of 200 mmol L^{-1} $CuSO_4$ was added to the mixture, followed by incubation at 4.0 °C for 18 h. The synthetic product were centrifuged and redispersed to remove the non-binding enzyme. Finally, ACC-HNFs were obtained by repeating the above process three times.

2.3. Manufacture of dual-modal biosensor

The 10 μL ACC-HNFs modified paper was directly added into the detection zone. Then, 10 μL of ACh, TMB, and stop solution was added into different regions in sequence. After 10 μL paraoxon was introduced into detection zone, region I, II, and III of the detection zone was folded and the fold of each region was maintained for 30 min, then a discernible colorimetric signal was observed with naked eyes in the hollow region. Meanwhile, the entire paper was folded above the electrodes, and the generated electrons can be better connected to the working electrode through the hollow region.

2.4. Electrochemical and colorimetric detection of paraoxon

All electrochemical measurement processes were performed at room temperature and each measurement was performed in a new disposable SPCE. Before the analysis of the paraoxon, parameters, such as ACh concentration, ACC-HNFs concentration, and incubation time, were further optimized. Amperometric i-t curves were recorded at +100 mV during 30 s. For colorimetric measurements, different concentrations of paraoxon were reacted with ACC-HNFs in the presence of 50 μL ACh, and 50 μL pH 7.5 Tris-HCl buffer at 37 °C. After 30 min, 50 μL TMB (1.5 mmol L^{-1} in DMSO), 900 μL deionized water, and 200 μL acetate buffer (0.1 mol L^{-1}, pH 4.0) were added into the mixture at room temperature for 15 min, the colorimetric changes were visually observed and also measured at 652 nm with the spectrophotometer. The detection mechanism of this dual-modal biosensor is based on inhibiting the activity of AChE, thus the inhibition rate (I%) can be expressed as a linear relationship with the concentration of paraoxon. I% was analyzed by the following relation:

$$I\% = (I_{\text{no inhibitor}} - I_{\text{inhibitor}}) / (I_{\text{no inhibitor}}) \times 100\% \quad (1)$$

Where $I_{\text{no inhibitor}}$ and $I_{\text{inhibitor}}$ represented the response (absorbance and current) of ACC-HNFs-TMB and ACC-HNFs-TMB-OPs system, respectively.

3. Results and discussion

3.1. Characterization of the AChE/ChO/$Cu_3(PO_4)_2$-HNFs

A one-pot process was applied to synthesize ACC-HNFs with good dispersion via protein biomimetic mineralization at the scaffold of $Cu_3(PO_4)_2$•$3H_2O$ (Fig. 1A). Hybrid-building blocks (AChE and ChO) in the form of complexes with Cu (II) by the coordination between the nitrogen atoms of the amide groups and metal ion. Following, nucleation of copper phosphate crystals ($Cu_3(PO_4)_2$•$3H_2O$) were formed at binding sites and grow to the separate petal-like structure (nanosheets, as shown in Fig. S1). Through the biomineralization, anisotropic growth and accumulation of nanosheets results in the formation of ACC-HNFs. As expected, ACC-HNFs exhibited three-dimensional flower-like morphology under SEM with an average size of 5.0 ± 0.7 μm (Fig. 1B and Fig. S2). The unique hierarchically structured nanoflowers with high specific surface area could effectively increase the recognition of the substrate molecules, thus contributed to the improvement of the biocatalytic activity of the ACC-HNFs. TEM image of single nanoflower further showed favorable hierarchical structure with a petal-like structure (Fig. 1C). Close observation clearly demonstrated that the light-colored petal portion were composed of nanoflake structures (Fig. 1D). The difference color of an individual ACC-HNFs in the energy dispersive spectroscopy (EDS) patterns expressed the elemental composition (C, P, and Cu elements) and distribution of the product, revealing the presence of enzymes and $Cu_3(PO_4)_2$ components in the nanoflowers (Fig. 1E). In this process, biocompatible $Cu_3(PO_4)_2$ plays a vital role in the immobilization of AChE and ChO. The FT-IR spectroscopy further proved the presence of PO_4^{3-}, in which the adsorption bands at around 1128 cm^{-1} associated with the stretching vibration of P = O units (Fig. 1F). The XRD patterns (Fig. S3) indicated that the major crystalline components for ACC-HNFs were $Cu_3(PO_4)_2$. Such protein assembly protocol is attractive for efficient construction of ACC-HNFs, owing to their simplicity of synthesis procedure without any toxic elements or complex purification pathways.

For enzyme-mediated signal amplification strategies in sensing pesticide, the core challenge is to carry numerus of enzyme molecular and maintain the catalytic bioactivity. To testify the loading capacity, TGA of the as-prepared ACC-HNFs was conducted in Fig. 1G. The first-stage decomposition of ACC-HNFs started from 210 °C and finished around 390 °C, which was attributed to the burning of enzyme, indicating the loading capacity for encapsulated enzyme of nanoflower was approximately 27.4%. To further elucidate that AChE and ChO were both immobilized on the organic-inorganic hybrid nanoflowers, rhodamine B (RhB)-labelled AChE (Red) and fluorescein isothiocyanate (FITC)-modified ChO (Green) were employed as building blocks for the synthesis of ACC-HNFs. In confocal fluorescence microscopy images, the green-emission dots and red-emission dots represented the distribution of ChO and AChE in the ACC-HNFs (Fig. 2A, B, 2C), respectively. The overlapped yellowish green color in the co-localization image is consistent with the internal integration of the two enzymes in the nanoflower carriers (Fig. 2D). Accordingly, by estimating the relative amount of enzyme in nanoflower (fluorescence method, Fig. S4) and the initial amount (mass feeding ratio of AChE:ChO) in the reaction, the enzyme immobilization efficiency of AChE and ChO was calculated to be 80.0% and 50.8%, respectively. Then, the activity of the immobilized AChE and ChO in the ACC-HNFs was carefully investigated by Ellman's test and potassium permanganate redox titration (Figs. S5 and S6). Compared with free enzymes, ACC-HNFs exhibit 8.7% and 29.7% decrease in the activity of the immobilized AChE and ChO, which may due to the mass-transfer limitations in the scaffold. Although there is a slight decrease in enzymatic activity, the storage stability of enzyme in ACC-HNFs reactor was significantly improved compared with that of two enzymes in homogeneous diffusional solution (Fig. 2E and F). The outstanding stability may be attributed to the biocompatible interface of $Cu_3(PO_4)_2$ for the enzyme immobilization. Because high enzymic activity and long-term stability conferred better catalytic efficiency, this designed ACC-HNFs indeed provided new possibilities for sensing application.

3.2. Peroxidase-mimetic activity of AChE/ChO/$Cu_3(PO_4)_2$-HNFs

Besides its high surface area, ACC-HNFs also showed a unique advantage of mimic-enzyme property. The potential peroxidase-like catalytic activity of ACC-HNFs was investigated by using several typical colorimetric substrates in the presence of H_2O_2. As displayed in Fig. 3A, the ACC-HNFs could catalyze the oxidation of 2,2′-azino-bis-(3-ethylbenzthiazoline-6-sulfonic acid) (ABTS), TMB, di-azo-aminobenzene (DAB), and o-phenylenediamine (OPD) to generate corresponding oxproduction with respective color changes, revealing that ACC-HNFs indeed exhibit the inherent peroxidase-like activity. To optimize the performance of ACC-HNFs, a series of control experiments were carried out (Fig. S7). The optimal conditions were determined as followed: the ACC-HNFs were synthesized at 4 °C for 18 h with pH 8.0 (Fig. 3B), which not only possessed high activity of nanozyme, but also brought benefit to maintain the activity of natural enzyme. The steady-state kinetic experiments were performed to further evaluate the peroxidase-like activity (Fig. S8). In a certain range of substrate concentration,

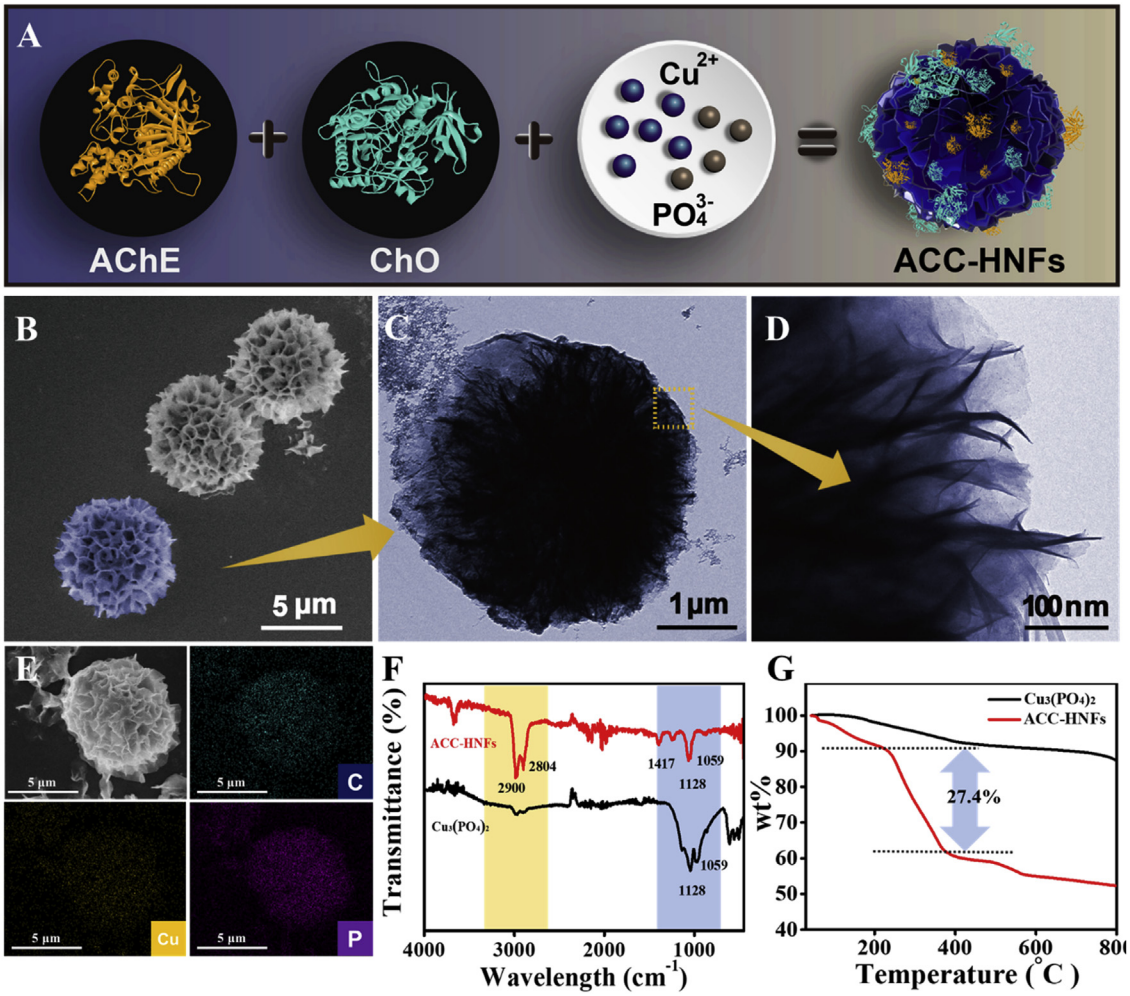

Fig. 1. (A) Synthetic process for the ACC-HNFs. The SEM (B) and TEM images (C) of the as-prepared nanoflowers. (D) Low-resolution TEM of the region. (E) EDS element patterns of the prepared nanoflowers. (F) FT-IR spectra of as-prepared ACC-HNFs and $Cu_3(PO_4)_2$. (G) TGA plots of the ACC-HNFs and $Cu_3(PO_4)_2$.

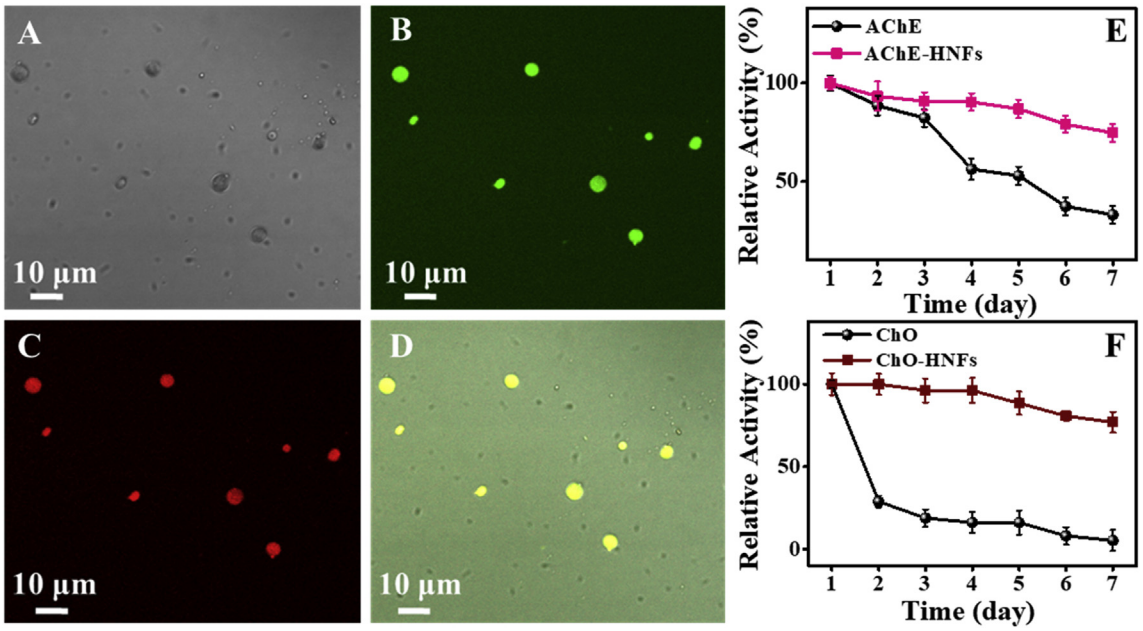

Figure 2. (A) Bright-field image of AChE-ChO-$Cu_3(PO_4)_2$ hybrid nanoflowers. (B) FITC labelled ChO in nanoflowers. (C) RhB labelled AChE in nanoflowers. (D) The overlap image of bright-field and fluorescence images. (E) Storage stability of AChE-HNFs compared with that of AChE in homogeneous diffusional solution. (F) Storage stability of ChO-HNFs compared with that of ChO in homogeneous diffusional solution.

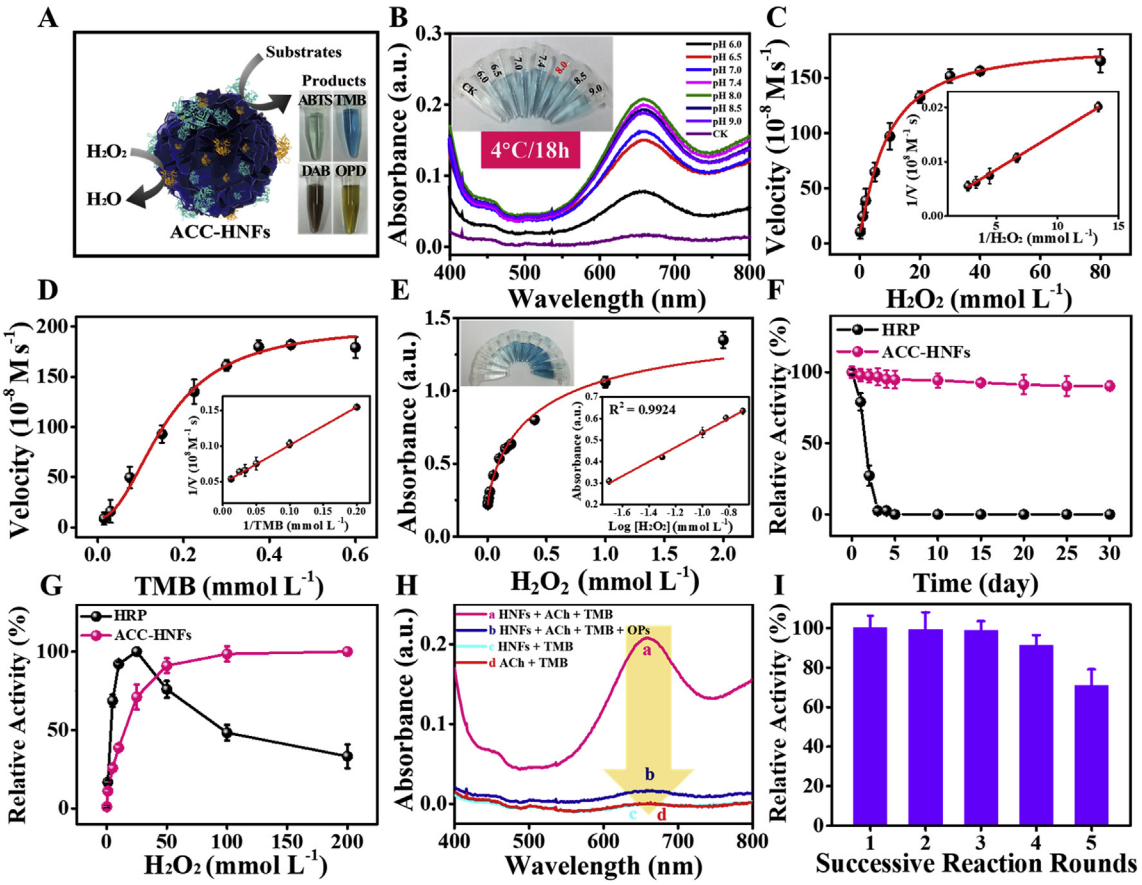

Fig. 3. (A) ACC-HNFs catalyzed the oxidation of peroxidase substrates to produce colorimetric reactions. (B) Optimizing the synthesis conditions of ACC-HNFs. (C) Michaelis-Menten and Lineweaver-Burk plots for H_2O_2 and (D) TMB. (E) The UV–Vis absorption spectra of the reaction solutions containing ACC-HNFs with different concentration of H_2O_2. (F) The enzymatic activity of ACC-HNFs and free HRP during storage for 30 days. (G) Effects of H_2O_2 concentration on the catalytic activities of ACC-HNFs and free HRP. (H) The UV–Vis absorption spectra of (a) HNFs + ACh + TMB (b) HNFs + ACh + TMB + OPs (c) ACC-HNFs + TMB and (d) ACh + TMB. (I) The circulation utilization rate of the ACC-HNFs.

typical Michaelis-Menten curves were determined for both TMB and H_2O_2 (Fig. 3C and D). Michaelis-Menten constant (K_m) value of the ACC-HNFs with both TMB (0.198) and H_2O_2 (0.324) as the substrate was much lower than that of horseradish peroxidase (HRP), indicating that ACC-HNFs exhibited a significantly stronger affinity toward substrates (Table S1). Potential enzymatic performance of ACC-HNFs was further investigated in detail by detecting H_2O_2. The results were depicted as Fig. 3E that the absorbance at 652 nm increased along with the increasing of H_2O_2 concentrations, accompanying that the system color gradually turned into deeper blue (Fig. 3E inset). Stability of nanomaterials is a main property to evaluate the performance in sensing. After 30 days of storage at room temperature, the activity of ACC-HNFs remained almost constant of their initial activity (~92%). In contrast, HRP showed a substantial loss of activity (~95% decrease in absorbance intensity) at the third day (Fig. 3F). Moreover, under extreme pH or high temperature, the nanozyme also kept relative high stability in aqueous solution (Fig. S9). The H_2O_2 concentration for suppressing the enzymic activity of nanozyme was at least 10-times higher than HRP, indicating that nanozyme possess extremely higher H_2O_2 tolerance compared with that of HRP (Fig. 3G). Those data clearly illustrating that the ACC-HNFs possessed acceptable mimic enzyme catalytic activity with excellent stability, providing considerable opportunities for constructing artificial enzyme cascade platform by integrating nanozyme and natural enzyme.

3.3. Colorimetric and electrochemical detection of paraoxon

To design a facile and accurate strategy for OPs (paraoxon as a model) detection, the artificial enzyme cascade platform was established based on ACC-HNFs. The feasibility of multi-enzyme cascade reaction was assessed in Fig. 3H. That is, ACC-HNFs with activity of natural enzyme (AChE and ChO) catalyzed ACh hydrolysis to produce choline, and subsequently converted to yield betaine and H_2O_2 by means of dissolved oxygen. In the presence of H_2O_2, ACC-HNFs further catalyzed the TMB into colored product oxTMB with characteristic absorbance at 652 nm (curve a). The equation of the reaction is shown below.

$$\text{Acetycholine chloride} + H_2O \xrightarrow{\text{AChE}} \text{Choline} + \text{Acetic acid} \quad (2)$$

$$\text{Choline} + O_2 \xrightarrow{\text{ChO}} \text{Beataine} + H_2O_2 \quad (3)$$

$$\text{TMB} + H_2O_2 \xrightarrow{\text{Nanoflower}} \text{oxTMB} + H_2O \quad (4)$$

When paraoxon was introduced, the AChE activity was immediately inhibited, which prevented the generation of H_2O_2, accompanying the absorbance change of system (curve b). Meanwhile, the solutions (substrate system) containing ACh or ACC-HNFs alone could not induce any change of absorbance intensity (curve c, d), indicating that ACC-HNFs-based artificial enzyme cascade platform could be used for sensing OPs. The stability of platform was further examined by cycle utilization. As shown in Fig. 3I, after five reaction cycles, the ACC-HNFs only lost 28% catalytic activity, which confirmed that the ACC-HNFs were recyclable and could be utilized for long-term operation. As shown in Fig. S10, there were no significant decrease for the activities of AChE, ChO, and nanozyme (19.7%, 17.2%, and 10.1%, respectively). Thus,

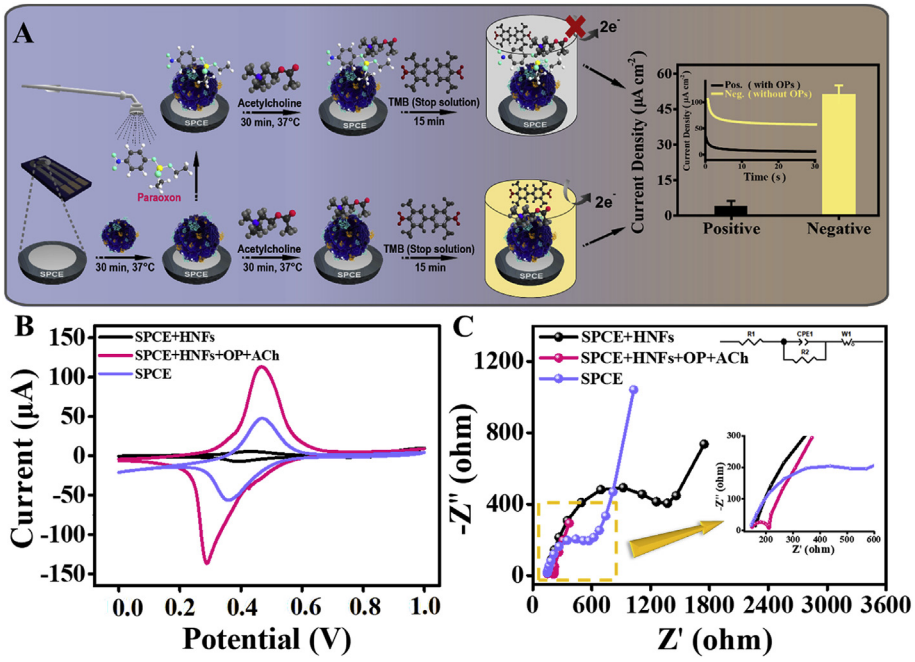

Fig. 4. (A) Immobilization of ACC-NHFs on the surface of SPCE and the inhibition effect of paraoxon on AChE. The response of amperometric current density for the negative (no paraoxon) and positive (with paraoxon) samples. The signal change of the CV (B) and EIS (C) for each modified layer of the as-prepared biosensor. The experimental conditions are as follows: For CV, scan potential is from −0.3 to +1.1 V, and scan rate is 0.1 V s^{-1}. For EIS, nanocomposites in a solution containing 0.1 mol L^{-1} KCl solution and 2.5 mmol L^{-1} $[Fe(CN)_6]^{3-}/[Fe(CN)_6]^{4-}$.

the decrease in the activity of ACC-HNFs was mainly due to the loss of the material during the process of centrifugal washing. Therefore, a facile and colorimetric biosensor was developed for the analysis of paraoxon via detecting the chromogenic substrate oxTMB.

It should be noted that TMB was not only the most common chromogenic substrate, but also regraded as electroactive redox dye indicator. For improving the sensing sensitivity, stop solution (2.0 mol L^{-1} HCl) was introduced, the blue colored oxTMB (charge transfer complex) turned to a yellow colored diimine (two-electron oxidation) with positive charge, which can be quantified by electrochemical detection methods. According to this performance, an electrochemical strategy for the detection of paraoxon was schematically represented in Fig. 4A. The ACC-HNFs were first deposited onto the screen-printed carbon electrode (SPCE) followed by the deposition of ACh layer before the final immobilization of TMB containing stop solution. When paraoxon was introduced, the activity of AChE was inhibited, resulting in a significantly decrease the response of amperometric current density. As a proof-of-concept, the electrochemical responses depicted that 5.04 μA cm^{-2} current was generated from the positive sample with OPs (Fig. 4A inset), which was 10 times lower than the negative control (55.43 μA cm^{-2}). Meanwhile, the corresponding color of solution changed from yellow to colorless (Fig. S11), which were consistent with the electrochemical measurements. Therefore, the feasibility for the detection of paraoxon was clearly verified by both amperometric and colorimetric readouts. To further investigate the stepwise immobilization process, the interface properties of modified SPCE was assessed by cyclic voltammetry (CV). As illustrated in Fig. 4B, the peak current of $[Fe(CN)_6]^{3-/4-}$ at the modification of SPCE with ACC-HNFs (black line) decreased greatly compared with that at bare SPCE (purple line), due to the limitation of electron-transfer caused by enzyme. Under the physical adsorption action, OPs and ACh were successfully fixed on the SPCE surface, accompanied by an increase in peak current (pink line). Electrochemical impendence spectroscopy (EIS) was further measured for investigating the electron-transfer resistance and interfacial changes of an SPCE electrode. Fig. 4C showed Nyquist diagrams changed gradually with the successive assembly of ACC-HNFs (black line) and ACC-HNFs/ACh/OPs (pink line), which was consistent with those in CV graph. The comparison between the CV and EIS measurement results for the bare SPCE and SPCE/ACC-HNFs, which indicated that the increase of impedance value corresponds the decrease of the peak current was associated with the immobilization of this poor electrically conductive material (ACC-HNFs). Thus, if ACC-HNFs were directly modified on the electrode, the electronic transmission of the reaction product would be hindered, which affected the sensitivity of the electrochemical biosensor. Furthermore, due to dark background color of SPCE, the color change of reaction was not easily observed. Thus, ACC-HNFs were gave priority to fix on the test paper instead of modifying it on the electrode, which made the electroactive product (diimine) directly contact with electrode, improving the sensitivity of electrochemical biosensor and achieving colorimetric sensing for OPs.

The dual-mode lab-on-paper device, containing of test-strips and SPCE, is elaborately designed by folding the specific tabs to form cross-shaped structure. Fig. S12 illustrated that the unique device comprised of one detection tab (ACC-NHFs section) in the center position surrounded by three folding regions that were modified with ACh, TMB, and stop solution. SEM images of bare paper and ACC-HNFs-modified detection zone were proved that the nanoflower had been successfully modified on the surfaces of cellulose fibers (Fig. S13). After specific folding in turn, the SPCE can be connected with detection zone (IV) to permit electrochemical response and visual prediction (Fig. S14). Under the optimal conditions (Figs. S15, S16, S17), the lab-on-paper device was used for monitoring paraoxon based on the dual-readout model. The naked-eye observation of noticeable color changes from yellow to colorless demonstrated the presence of paraoxon. As displayed in Fig. 5A, along with the paraoxon concentrations increasing from 0.01 to 100 ng mL^{-1}, the absorption at 452 nm of the ACC-HNFs/TMB system was decreased gradually. The linear regression equation was estimated to be I% = 10.147 Log [Paraoxon] + 21.834 (R^2 = 0.9990) with the detection limit (LOD) down to 10 pg mL^{-1}. It should be pointed out that our eyes' sensitivity could distinguish the obvious color variations for the semi-quantitative detection of paraoxon only reach 0.5 μg mL^{-1} (Fig. S18). Notably, the diimine product was electroactive, which allows the accurate quantification of paraoxon via electrochemical signal. In the case of the amperometric readout, a good linear relationship between I% and the concentration of paraoxon was obtained (Fig. 5B). The linear regression equation was estimated as I% = 12.296 Log [Paraoxon] + 66.471 (R^2 = 0.9910), which confirmed the relatively better sensitivity in the range of 6.0×10^{-6} – 0.6 ng mL^{-1} (LOD of 6.0 fg mL^{-1}) in comparison to the colorimetric output. Furthermore,

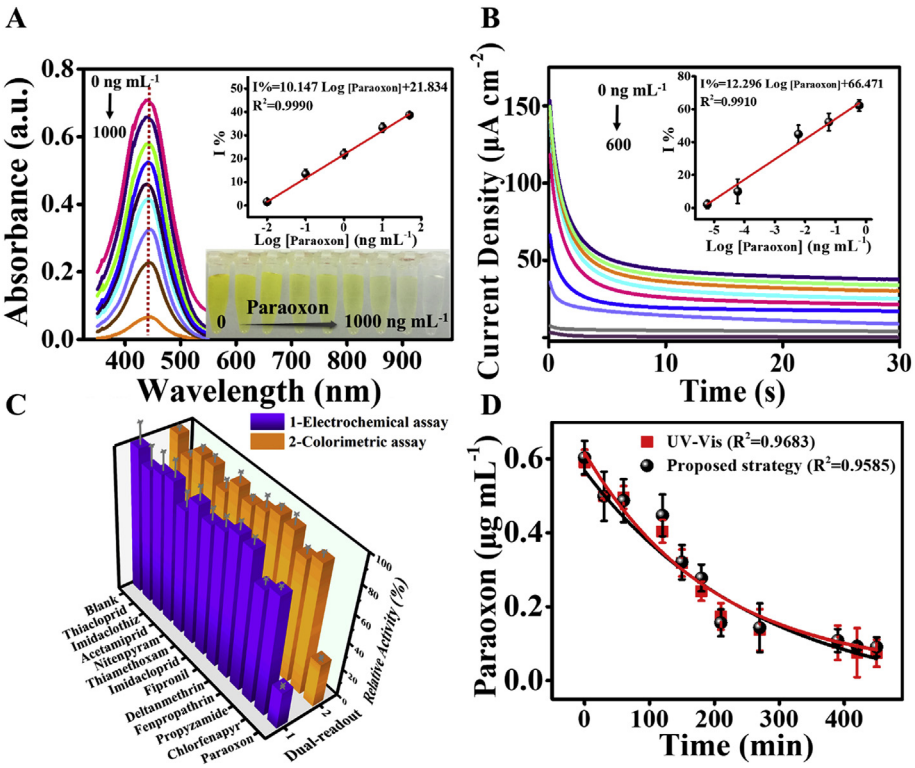

Fig. 5. (A) The absorption spectra of the oxidation product of TMB in the presence of various paraoxon concentrations. (Inset: the linear relationship between the absorbance at 452 nm and the paraoxon concentration. The images of the production of colored products for different concentrations of paraoxon. (B) Amperometric currents obtained for the designated concentration of paraoxon. (Inset: the corresponding linear regression curves). (C) Selectivity of the dual-readout device toward different substances. (D) The degradation curve of paraoxon by conventional method (UV–Vis) and the proposed strategy.

because of ACC-HNFs could catalyze H_2O_2 to produce electroactive product (•OH), a control experiment for paraoxon detection was designed without introducing TMB. For direct comparison, the sensitivity of ACC-HNFs system against ACC-HNFs/TMB system was performed by using the same set of solution and analyte (Fig. S19). It is worth noting that ACC-HNFs/TMB system possessed high sensitivity, which was ascribed to the high electroactive and acceptable stability of diimine. This duel-model platform offered two different detection alternatives: one produced by the yellow color of diimine product (qualitative mode) and the other output passed via electrochemical signal (high-sensitivity quantitative mode), achieving an "on-demand" tuning of the monitoring performance. It should be noted that the qualitative mode is more convenient than the quantitative mode because the latter required an additional electrochemical operation. For POCT application, qualitative mode performed priority in sensing unknown sample. High-sensitivity quantitative mode was only needed when no effective signal was obtained in qualitative mode.

In addition, a comparison with other related OPs sensors showed that our developed dual-readout biosensor performed outstanding analytical performance with a satisfactory LOD, broader linear range, and acceptable detection time. It is worth mentioning that the ability to detect pesticides at fg mL^{-1} level is sufficient to detect them at residue level according to the generally accepted standards of many organizations around the world (Cheng et al., 2018). Furthermore, the proposed dual-readout platform whose sensitivity is at least one order of magnitude higher than many of the previous electrochemical biosensors (Table S2). This ultralow detection limit arises from the following distinctive features: (1) ACC-HNFs as carrier can load amount of AChE and ChO by taking advantage of large specific surface area, which not only maintain the catalytic activity of enzyme, but also improve the stability of protein. (2) ACC-HNFs as nanozyme exhibited much higher catalytic activity than natural enzyme (HRP), achieving enhanced output signal. (3) The high-performance artificial enzyme cascade system made AChE and ChO closer to reduce the substrate diffusion and decomposition, shorten the distance of electronic transfer, thus the electrochemical signal can be amplified remarkably. (4) The sensitive electrochemical signal was also related to the positively charged diimine that possessed high electroactive, improving electrochemical signal of the platform.

Selectivity is a vital characteristic in assessing the ability of the developed biosensor, particularly for POCT application. To better simulate the actual environment for monitoring paraoxon, the interference of the non-OPs (pyrethroid pesticide, neonicotinoid pesticide and arylpyrrole pesticide) was investigated. As revealed in Fig. 5C, the output signal exhibited remarkable decrease toward paraoxon (0.1 ng mL^{-1}). In contrast, there were no significant signal changes after adding above interference pesticide (200 ng mL^{-1}). As shown in Fig. S20, some related sulfur atom-containing compounds (100 ng mL^{-1}) also did not produce interference signals, indicating the high selectivity of artificial enzyme cascade system. Furthermore, to investigate the universality of artificial enzyme cascade system, the responses of seven typical kinds of OPs (0.1 ng mL^{-1}) were compared with paraoxon (Fig. S21). Meanwhile, the dual-response signals of each OPs were decreased to different degrees, but the decrease trend of paraoxon was the maximum among of OPs. The above results confirmed that the proposed sensing platform could be utilized for monitoring a variety of OPs.

3.4. Real sample analysis

Subsequently, in order to check the potential feasibility of the dual-readout platform applied for environmental and agricultural samples analysis, the concentrations of paraoxon in real sample, including tap water, river water, rice, and apple were evaluated through the standard addition method. In this case, the samples were spiked with paraoxon standard at the concentration of 5.0, 10.0, and 20.0 ng mL^{-1} (Please see supporting information for details). As summarized in Table S3, the electrochemical readout obtained excellent recoveries (82.6–112.1%) with relative standard deviations (RSD) lower than 4.3%, suggesting the potential applicability of the established platform for the analysis of paraoxon in complex real samples. Notably, the degradation of paraoxon under simulated-sunlight applied to authentic pear samples were monitored by conventional method (UV–Vis) and the proposed strategy

(Fig. 5D). The dissipation of paraoxon apparently followed pseudo first order kinetics. The dual-readout platform results for analyzing pesticide showed acceptable agreement (a correlation coefficient $R^2 = 0.9859$) with UV–Vis installed in the standard laboratory of testing agency, demonstrating the good reliability and feasibility of dual-readout platform for monitoring pesticide residues.

4. Conclusion

In summary, we have proposed an innovative and facile strategy for the biomimetic mineralization assembly of all-in-one ACC-HNFs integrating the functions of natural enzyme and nanozyme. Employed the ACC-HNFs to fabricate high-performance artificial enzyme cascade system, a portable lab-on-paper biosensor with dual electrochemical and colorimetric signal readout was successfully constructed for sensitive and reliable paraoxon detection. Compared with traditional single modality analysis methods, this dual-readout POCT platform based on artificial enzyme cascade system possesses the following advantages: (1) In the artificial enzyme cascade system, ACC-HNFs exhibited high catalytic activity, which can be ascribed to the large specific surface area to reduce the substrate diffusion and shorten the distance of electron transfer. These meticulously designed ACC-HNFs provide a one-pot assembly strategy to fabricate high-performance artificial enzyme cascade system that open an avenue for integrating signal amplification unit and biorecognition element. (2) Our approach integrates electrochemistry and colorimetric patterns into one system for “on-demand” detecting OPs. The results of the analysis not only can be preliminarily screened by observing the obvious color changes with naked eyes, but also can be accurately quantified by electrochemical signals with significantly improved sensitivity. More importantly, the two groups of results can mutually authenticate, which can effectively avoid false positive and negative detection. (3) This paper-based biosensor dispenses with complex sample pretreatment or sophisticated instruments, which makes it suitable for on-site monitoring, displaying important features enabling applications prospect in POCT for other harmful substances.

CRediT authorship contribution statement

Rui Jin: Conceptualization, Data curation, Formal analysis, Investigation, Methodology, Resources, Software, Visualization, Writing - original draft, Writing - review & editing. **Deshuai Kong:** Data curation, Formal analysis, Investigation, Resources, Software, Visualization, Writing - original draft. **Xu Zhao:** Data curation, Formal analysis, Investigation, Resources, Software, Validation, Writing - original draft. **Hongxia Li:** Data curation, Formal analysis, Investigation, Resources, Software, Validation, Writing - original draft. **Xu Yan:** Conceptualization, Data curation, Formal analysis, Funding acquisition, Investigation, Methodology, Project administration, Resources, Supervision, Writing - review & editing. **Fangmeng Liu:** Data curation, Formal analysis, Methodology. **Peng Sun:** Data curation, Formal analysis, Funding acquisition, Methodology. **Dan Du:** Formal analysis, Methodology. **Yuehe Lin:** Formal analysis, Methodology, Project administration, Supervision. **Geyu Lu:** Conceptualization, Funding acquisition, Project administration, Supervision.

Acknowledgements

This work was supported by the National Key Research and Development Program of China (Grant Numbers 2016YFC0207300). National High-tech Research and Development Program of China (Grant Numbers 2014AA06A505). The National Nature Science Foundation of China (Grant Numbers 61831011, 61833006, 61722305 and 21806051). Program for JLU Science and Technology Innovative Research Team (JLUSTIRT 2017TD-07). Science and Technology Development Program of Jilin Province (Grant Numbers 2017052016JH). The Fundamental Research Funds for the Central Universities. The National Postdoctoral Program for Innovative Talents (Grant Numbers BX201700096). The Graduate Innovation Fund of Jilin University (Grant Numbers 101832018C016).

Appendix A. Supplementary data

Supplementary data to this article can be found online at https://doi.org/10.1016/j.bios.2019.111473.

Declaration of interests

The authors declare that they have no known competing financial interests or personal relationships that could have appeared to influence the work reported in this paper.

References

Aragay, G., Pino, F., Merkoçi, A., 2012. Chem. Rev. 112 (10), 5317–5338.
Cequier, E., Sakhi, A.K., Haug, L.S., Thomsen, C., 2016. J. Chromatogr. A 1454, 32–41.
Chen, A., Chatterjee, S., 2013. Chem. Soc. Rev. 42 (12), 5425–5438.
Chen, H., Zhang, H., Yuan, R., Chen, S., 2017. Anal. Chem. 89 (5), 2823–2829.
Cheng, N., Song, Y., Fu, Q., Du, D., Luo, Y., Wang, Y., Xu, W., Lin, Y., 2018. Biosens. Bioelectron. 117, 75–83.
Cui, H.-F., Wu, W.-W., Li, M.-M., Song, X., Lv, Y., Zhang, T.-T., 2018. Biosens. Bioelectron. 99, 223–229.
Ge, J., Lei, J., Zare, R.N., 2012a. Nat. Nanotechnol. 7, 428.
Ge, L., Yan, J., Song, X., Yan, M., Ge, S., Yu, J., 2012b. Biomaterials 33 (4), 1024–1031.
Gupta, R.D., Goldsmith, M., Ashani, Y., Simo, Y., Mullokandov, G., Bar, H., Ben-David, M., Leader, H., Margalit, R., Silman, I., Sussman, J.L., Tawfik, D.S., 2011. Nat. Chem. Biol. 7, 120.
Huang, Y., Ran, X., Lin, Y., Ren, J., Qu, X., 2015. Chem. Commun. 51 (21), 4386–4389.
Kaur, N., Prabhakar, N., 2017. Trac. Trends Anal. Chem. 92, 62–85.
Khare, S.D., Kipnis, Y., Greisen Jr., P., Takeuchi, R., Ashani, Y., Goldsmith, M., Song, Y., Gallaher, J.L., Silman, I., Leader, H., Sussman, J.L., Stoddard, B.L., Tawfik, D.S., Baker, D., 2012. Nat. Chem. Biol. 8, 294.
Liebes-Peer, Y., Rapaport, H., Ashkenasy, N., 2014. ACS Nano 8 (7), 6822–6832.
Maliyekkal, S.M., Sreeprasad, T.S., Krishnan, D., Kouser, S., Mishra, A.K., Waghmare, U.V., Pradeep, T., 2013. Small 9 (2), 273–283.
Miao, L., Zhu, C., Jiao, L., Li, H., Du, D., Lin, Y., Wei, Q., 2018. Anal. Chem. 90 (3), 1976–1982.
Nasir, M.Z.M., Mayorga-Martinez, C.C., Sofer, Z., Pumera, M., 2017. ACS Nano 11 (6), 5774–5784.
Palmer, M.J., Moffat, C., Saranzewa, N., Harvey, J., Wright, G.A., Connolly, C.N., 2013. Nat. Commun. 4, 1634.
Pang, Z., Hu, C.-M.J., Fang, R.H., Luk, B.T., Gao, W., Wang, F., Chuluun, E., Angsantikul, P., Thamphiwatana, S., Lu, W., Jiang, X., Zhang, L., 2015. ACS Nano 9 (6), 6450–6458.
Shen, H., Qu, F., Xia, Y., Jiang, X., 2018. Anal. Chem. 90 (6), 3697–3702.
Si, P., Ding, S., Yuan, J., Lou, X.W., Kim, D.-H., 2011. ACS Nano 5 (9), 7617–7626.
Szyszko, B., Białońska, A., Szterenberg, L., Latos-Grażyński, L., 2015. Angew. Chem. 127 (16), 5014–5018.
Tang, H., Yan, F., Lin, P., Xu, J., Chan, H.L.W., 2011. Adv. Funct. Mater. 21 (12), 2264–2272.
Uth, C., Zielonka, S., Hörner, S., Rasche, N., Plog, A., Orelma, H., Avrutina, O., Zhang, K., Kolmar, H., 2014. Angew. Chem. Int. Ed. 53 (46), 12618–12623.
Wang, J., Dai, J., Xu, Y., Dai, X., Zhang, Y., Shi, W., Sellergren, B., Pan, G., 2019. Small 15 (1), 1803913.
Winrow, C.J., Hemming, M.L., Allen, D.M., Quistad, G.B., Casida, J.E., Barlow, C., 2003. Nat. Genet. 33, 477.
Wu, T., Yang, Y., Cao, Y., Song, Y., Xu, L.-P., Zhang, X., Wang, S., 2018. ACS Appl. Mater. Interfaces 10 (49), 42050–42057.
Yan, X., Li, H., Su, X., 2018a. Trac. Trends Anal. Chem. 103, 1–20.
Yan, X., Song, Y., Wu, X., Zhu, C., Su, X., Du, D., Lin, Y., 2017. Nanoscale 9 (6), 2317–2323.
Yan, X., Song, Y., Zhu, C., Li, H., Du, D., Su, X., Lin, Y., 2018b. Anal. Chem. 90 (4), 2618–2624.
Yang, M., Choi, B.G., Park, T.J., Heo, N.S., Hong, W.H., Lee, S.Y., 2011. Nanoscale 3 (7), 2950–2956.
Ye, R., Zhu, C., Song, Y., Lu, Q., Ge, X., Yang, X., Zhu, M.-J., Du, D., Li, H., Lin, Y., 2016. Small 12 (23), 3094–3100.
Yu, X., Biedrzycki, A.H., Khalil, A.S., Hess, D., Umhoefer, J.M., Markel, M.D., Murphy, W.L., 2017. Adv. Mater. 29 (33), 1701255.
Zhao, F., Wu, J., Ying, Y., She, Y., Wang, J., Ping, J., 2018. Trac. Trends Anal. Chem. 106, 62–83.
Zhu, J., Wen, M., Wen, W., Du, D., Zhang, X., Wang, S., Lin, Y., 2018. Biosens. Bioelectron. 120, 175–187.
Zou, Y., Zhang, Y., Xu, Y., Chen, Y., Huang, S., Lyu, Y., Duan, H., Chen, Z., Tan, W., 2018. Anal. Chem. 90 (22), 13687–13694.